Chinese Journal of
POLYMER SCIENCE

RESEARCH ARTICLE

https://doi.org/10.1007/s10118-026-3765-8
Chinese J. Polym. Sci.

Flow-induced Structural Evolution in Graphene Oxide-grafted Carbon Nanotube/Polyamide 6 Composites with Enhanced Barrier Performance, Mechanical Properties, and Thermal Conductivity

Guan-Jun Liu[a*], Mei-Ling Yan[b*], Zhen Tian[a], Lu Wang[c], Fan Yang[d], and Rong-Guo Wang[d]

[a] *College of chemical engineering and materials, Shandong University of Aeronautics, Binzhou 256603, China*
[b] *School of Materials Science and Engineering, Nanchang Hangkong University, Nanchang 330063, China*
[c] *Department of Geology and Surveying and Mapping, Shanxi Institute of Energy, Jinzhong 030600, China*
[d] *National Key Laboratory of Science and Technology on Advanced Composites in Special Environments, Harbin Institute of Technology, Harbin 150001, China*

Electronic Supplementary Information

Abstract Hot pressing is widely used to tailor the structures and properties of polymer composites. However, how it drives structural evolution and thereby affects barrier, mechanical, and thermal properties remains insufficiently understood. In this work, graphene oxide-grafted carbon nanotube/polyamide 6 (GO-*g*-CNT/PA6) composites were subjected to hot pressing at different radial expansion ratios (ε=0, 2, and 4) to investigate the flow-induced structural evolution and the resulting property changes. Scanning electron microscopy and transmission electron microscopy observations revealed that hot pressing promoted the rearrangement and preferential alignment of the hybrid nanofillers, while two-dimensional wide-angle X-ray diffraction confirmed the enhanced crystalline orientation after hot pressing. Differential scanning calorimetry showed increased crystallinity in both the neat PA6 and GO-*g*-CNT/PA6 composites. Representative positron annihilation lifetime spectroscopy analysis further indicated a reduction in the fractional free volume, whereas the characteristic size of individual free-volume holes remained nearly unchanged. The results indicate that the optimal hot-pressing condition is property-dependent. A moderate deformation at ε=2 is more favorable for improving the hydrogen barrier and tensile properties, whereas a stronger deformation at ε=4 is more effective in promoting in-plane heat transport. These findings establish a correlation between the processing, structural evolution, and multifunctional properties of GO-*g*-CNT/PA6 composites, providing guidance for the design of PA6-based liner materials for Type IV hydrogen storage vessels.

Keywords Hot pressing; Polyamide 6 composites; Hybrid nanofillers; Structural evolution; Hydrogen permeability

Citation: Liu, G. J.; Yan, M. L.; Tian Z.; Wang L.; Yang F.; Wang R. G. Flow-induced structural evolution in graphene oxide-grafted carbon nanotube/polyamide 6 composites with enhanced barrier performance, mechanical properties, and thermal conductivity. *Chinese J. Polym. Sci.* https://doi.org/10.1007/s10118-026-3765-8

INTRODUCTION

The rapid development of high-pressure hydrogen storage technology has imposed increasingly stringent demands on the use of polymer liners in Type IV hydrogen storage vessels.[1–3] In such systems, the liner is expected not only to suppress hydrogen leakage but also to maintain dimensional stability and structural reliability under repeated pressure and temperature fluctuations. Therefore, liner materials must simultaneously satisfy the requirements of low hydrogen permeability, sufficient mechanical robustness, and reasonable thermal transport capability.[4,5] Polyamide 6 (PA6), a representative engineering thermoplastic, has attracted sustained interest because of its balanced mechanical properties, good processability, and relatively favorable gas barrier performance compared with many conventional polymers.[6–8] However, the intrinsic performance of neat PA6 still falls short of the increasingly demanding requirements of practical hydrogen storage applications, especially when barrier, mechanical, and thermal properties need to be improved in a coordinated manner.[9] In this regard, Kis and Kókai identified permeability and thermomechanical properties as key factors affecting liner collapse in Type IV hydrogen storage vessels.[10]

A common strategy to improve the overall performance of PA6 is the introduction of nanoscale fillers, such as graphene,[11] boron nitride nanosheets (BNNS),[12] montmorillonite,[13] *etc*. Carbon-based nanofillers are particularly attractive because they can simultaneously affect the gas diffusion, stress transfer, and heat conduction. For example, graphene oxide (GO) has been widely used in polymer matrices to improve barrier performance owing to its high aspect ratio and platelet geometry, which can increase the tortuosity of the gas diffusion pathways.[14] On the other hand, carbon nanotubes (CNTs) are often employed to enhance mechanical

* Corresponding authors, E-mail: liuguanjun@sdua.edu.cn (G.J.L.)
E-mail: yanmeiling123@163.com (M.L.Y.)
Received April 26, 2026; Accepted May 31, 2026; Published online August 19, 2026

and thermal properties because of their excellent intrinsic stiffness and thermal conductivity.[15] Their Young's modulus is generally reported at the TPa level, and their intrinsic thermal conductivity is commonly reported to be on the order of 3000 $W \cdot m^{-1} \cdot K^{-1}$.[16,17] Nevertheless, the use of a single nanofiller often fails to deliver a desirable balance among multiple target properties. In many cases, sheet-like nanofillers are highly effective for barrier enhancement, whereas tubular nanofillers may enhance mechanical properties or heat transport but are more susceptible to aggregation and nonuniform dispersion.[18,19] To address these limitations, hybrid nanofillers combining nanostructures with different geometries have received increasing attention.[20,21] By integrating the planar barrier effect of GO with the bridging and heat-conduction functions of CNTs, hybrid architectures are expected to regulate the microstructure and properties more effectively than individual nanofillers. In principle, such hybrid nanofillers can improve interfacial interactions, facilitate network formation, and create more effective pathways for stress transfer and heat conduction while also maintaining a tortuous route for gas diffusion.[22,23] In our previous work, GO-grafted CNT hybrid nanofillers, denoted as GO-*g*-CNT, were incorporated into PA6 through *in situ* polymerization.[24] That study demonstrated that the covalently bonded hybrid nanofiller could more effectively improve the mechanical and thermal properties of PA6 than single nanofiller systems, thereby confirming the advantage of the GO-*g*-CNT architecture itself. However, previous studies have mainly focused on the nanofiller design and composition effects in unpressed composites. The role of subsequent processing in further reorganizing this hybrid architecture and regulating the coupled barrier, mechanical, and thermal properties remains unclear.

For semicrystalline polymer composites, the final properties are not solely determined by the nanofiller type and loading level. Post-processing can significantly affect nanofiller arrangement, polymer chain packing, and free-volume characteristics, thereby governing the relationship between the structure and properties of the material.[25,26] This issue is particularly important for hydrogen barrier applications because gas transport in polymers is strongly affected by crystalline orientation, crystallinity, and free volume.[27–29] At the same time, the mechanical response and thermal transport behavior of polymer composites are highly sensitive to structural anisotropy.[30] In other words, a processing method capable of regulating the structure across multiple length scales may provide a more effective route to achieving balanced multifunctional performance than nanofiller introduction alone. A recent study by Durand *et al.* showed that gas permeability in semicrystalline polymers depends not only on crystallinity, but also on the semi-crystalline microstructure, highlighting the importance of structural regulation in gas transport.[31] In addition, recent reviews by Ho *et al.* and Li *et al.* have emphasized that nanofiller orientation can strongly affect the anisotropic mechanical and thermal properties of polymer composites.[32,33] Studies by Song and coworkers further showed that structural alignment induced by processing can improve thermal management and mechanical performance in polymer composites, as demonstrated in oriented cellulose/BNNS films and laminated polypropylene/reduced GO hybrid films.[34,35] Among the various post-processing strategies, hot pressing is particularly attractive because it is a straightforward and scalable process that can generate a squeezing-flow field[36] thereby driving the anisotropic structural evolution of both the matrix and nanofillers. During radial expansion under compression, high-aspect-ratio nanofillers may rotate, rearrange, and align along preferred directions, whereas polymer chains and crystals may undergo flow-induced rearrangement, leading to changes in the crystalline orientation, crystallization behavior, and free volume. This flow-induced structural evolution is expected to simultaneously influence multiple properties. Specifically, aligned nanofillers and ordered crystalline structures may increase the tortuosity of hydrogen diffusion, improve load transfer efficiency, and promote directional heat conduction. Therefore, hot pressing is not merely a shaping process but also a potentially effective strategy for regulating the internal structure of multifunctional polymer composites.

Despite this potential, several key issues of hybrid PA6 composites remain insufficiently understood. First, previous studies have often focused on either nanofiller design or a single-target property, whereas the coupled evolution of nanofiller alignment, crystalline orientation, crystallization behavior, and free volume under hot pressing has rarely been systematically examined in a unified framework. Second, the structural responses of the hybrid nanofillers and the polymer matrix may not evolve synchronously with increasing deformation. A processing condition that favors a clearer nanofiller alignment does not necessarily lead to the highest crystalline orientation or the most favorable crystallization behavior. Consequently, the optimum conditions for barrier performance may differ from those for mechanical reinforcement or thermal transport. Third, for liner-related materials used in Type IV hydrogen storage vessels, it is particularly important to identify how processing regulates the balance among barrier, mechanical, and thermal properties rather than optimizing only one of them. Although previous studies have reported improvements in barrier, mechanical, or thermal properties individually, a systematic understanding of how hot pressing simultaneously regulates these properties is still lacking. In particular, the optimum processing conditions may be property-dependent rather than universal.

Based on these considerations, GO-*g*-CNT/PA6 composites serve as a suitable model system for examining how flow-induced structural evolution affects the multifunctional performance. In this system, the GO component can act as an effective barrier nanofiller, the CNT component can contribute to mechanical reinforcement and heat transport, and the PA6 matrix provides a semicrystalline platform whose crystalline orientation and crystallization behavior are highly sensitive to processing. In addition, the free-volume characteristics of PA6-based composites are influenced by both interfacial interactions and post-processing history, making this system particularly suitable for correlating the gas barrier behavior with structural evolution across different structural features. In this study, GO-*g*-CNT/PA6 composites were subjected to hot pressing at different radial expansion ratios (ε) to investigate the relationship between flow-induced structural evolution and multifunctional properties. Structural changes in the matrix and hybrid nanofillers were systematically character-

https://doi.org/10.1007/s10118-026-3765-8

ized using scanning electron microscopy (SEM), transmission electron microscopy (TEM), Raman mapping, two-dimensional wide-angle X-ray diffraction (2D-WAXD), differential scanning calorimetry (DSC), and positron annihilation lifetime spectroscopy (PALS). On this basis, the hydrogen permeability, tensile properties, and directional thermal conductivity were correlated with nanofiller alignment, crystalline orientation, crystallization behavior, and free-volume evolution. The present work aims to establish a clear correlation among the processing, structure, and properties of hot-pressed GO-*g*-CNT/PA6 composites, with particular emphasis on the coordinated regulation of barrier, mechanical, and thermal transport properties.

MATERIALS AND METHODS

Materials

GO nanosheets (8–15 μm in lateral size) and hydroxyl-functionalized CNTs (10–20 nm in outer diameter, 10–30 μm in length, and 3.06 wt% hydroxyl groups) were supplied by the Chengdu Institute of Organic Chemistry, Chinese Academy of Sciences (China). Other chemicals, including (3-aminopropyl)triethoxysilane (APTES), *N*-(3-dimethylaminopropyl)-*N*'-ethylcarbodiimide hydrochloride, 1-hydroxybenzotriazole monohydrate, *N*,*N*-diisopropylethylamine, dibutyltin dilaurate, hexamethylene diisocyanate (HDI), ε-caprolactam, sodium hydroxide, toluene-2,4-diisocyanate, glacial acetic acid, *N*,*N*-dimethylformamide (DMF), and ethanol, were purchased from Aladdin Biochemical Technology Co., Ltd. (Shanghai, China) and used as received without further purification.

Preparation of HDI-modified GO-*g*-CNT Hybrid Nanofillers

The hybrid nanofillers were constructed according to the procedures described in our previous work.[24] A schematic illustration of the preparation process is shown in Fig. 1(a). Firstly, 0.2 g of GO was dispersed in 50 mL of DMF and sonicated for 15 min to obtain a uniform suspension. Subsequently, 0.08 g of *N*-(3-

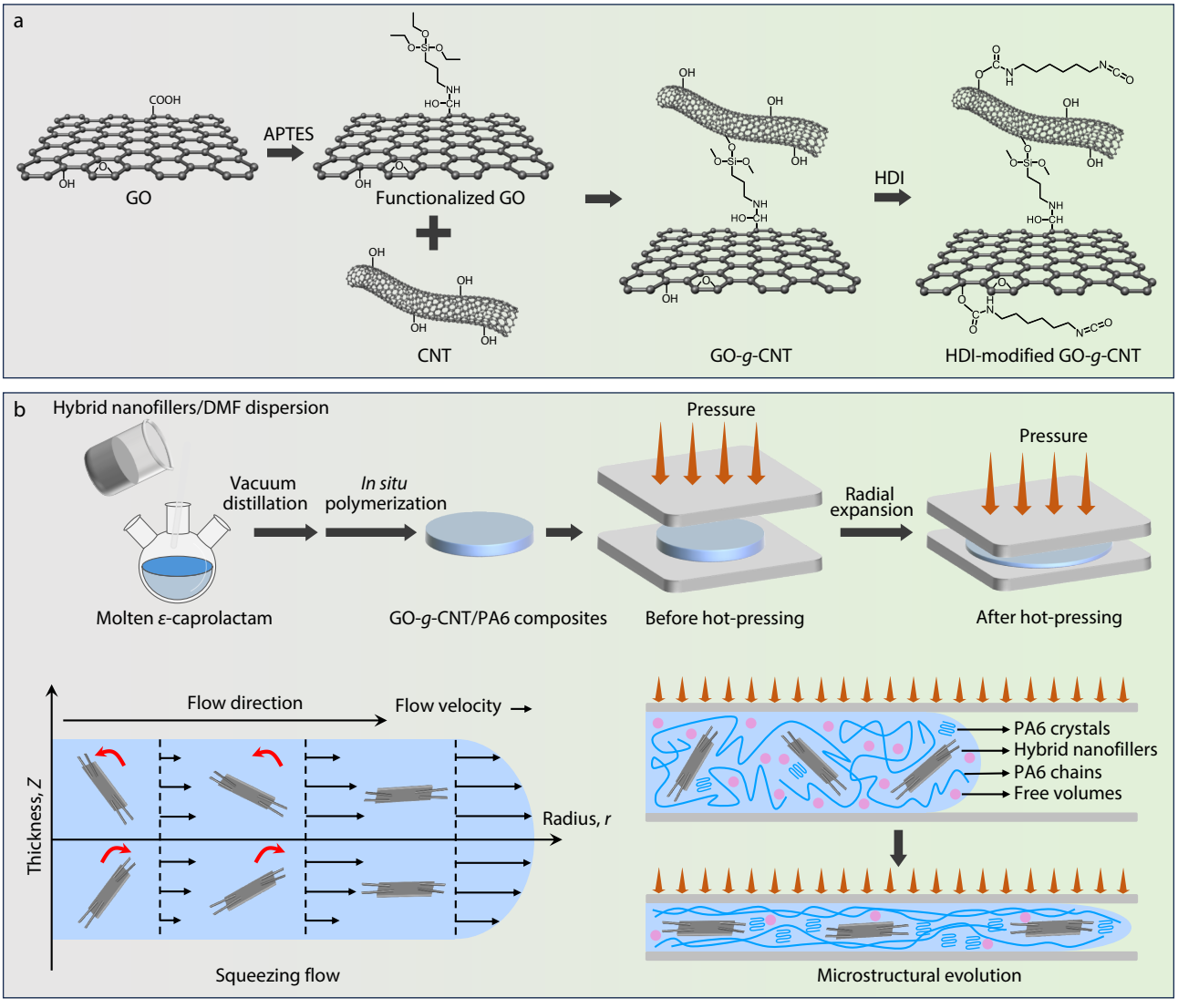

Fig. 1 Schematic illustration of (a) the preparation of HDI-modified GO-*g*-CNT hybrid nanofillers, and (b) the fabrication of GO-*g*-CNT/PA6 composites together with the hot-pressing induced squeezing flow, orientation, and microstructural evolution.

https://doi.org/10.1007/s10118-026-3765-8

dimethylaminopropyl)-*N*′-ethylcarbodiimide hydrochloride, 0.08 g of 1-hydroxybenzotriazole monohydrate, and 0.89 g of *N*,*N*'-diisopropylethylamine were added to activate the carboxyl groups on GO. APTES (0.4 g) was then added with stirring, and the mixture was maintained at 60 ℃ under nitrogen for 24 h to enable the reaction between the GO carboxyl groups and amine groups of APTES. The product was isolated by filtration and thoroughly washed with deionized water, ethanol, and DMF.

To construct the GO-*g*-CNT hybrid, the silane-modified GO and CNT were mixed at a mass ratio of 5:4 and resuspended in a DMF/deionized water mixture (9/1, *V*/*V*). A small amount of water was added to facilitate silane hydrolysis, and the pH was adjusted to 3–4 using glacial acetic acid to suppress siloxane condensation. The suspension was refluxed at 60 °C for 16 h to enable grafting between the GO and CNT, and the product was then washed sequentially with ethanol, deionized water, and DMF.

For HDI grafting, 0.1 g of GO-*g*-CNT was resuspended in DMF and then 3.0 g of HDI and three drops of dibutyltin dilaurate were introduced. The mixture was stirred at 60 °C under nitrogen for 1 h to functionalize the remaining hydroxyl groups with HDI. The product was collected by filtration through a polytetrafluoroethylene (PTFE) membrane and washed thoroughly with DMF to remove any unreacted HDI.

Preparation of GO-*g*-CNT/PA6 Composites

For the preparation of PA6 composites, 20.0 g of ε-caprolactam was melted at 80 ℃, followed by the addition of the DMF dispersion of the HDI-modified hybrid. After the complete removal of DMF under reduced pressure, 0.03 g of sodium hydroxide was introduced, and the mixture was heated to 135 ℃ under high vacuum to initiate anionic ring-opening polymerization. After 30 min, 0.115 g of toluene-2,4-diisocyanate was added to further lower the polymerization initiation temperature. The mixture was then rapidly and thoroughly stirred to ensure a uniform distribution before being cast into a mold preheated to 160 ℃ and maintained under vacuum for 1 h. Upon cooling to ambient temperature, the resulting GO-*g*-CNT/PA6 circular discs were ready for subsequent hot-press orientation studies. Previous studies have shown that composites with 0.5 wt% nanofiller exhibit relatively high tensile strength and satisfactory elongation at break, demonstrating good toughness. Therefore, this concentration was selected in the present work as a representative composition for investigating the effect of hot pressing on structural evolution and multifunctional properties.

Hot-press Induced Orientation of GO-*g*-CNT/PA6 Composites

The demolded composite sheets were hot-pressed into circular discs of defined diameters. The ratio of the final diameter to the initial diameter was defined as the radial expansion ratio, ε, and two levels were employed in this study, namely ε=2 and 4. Hot pressing was performed at 195 ℃ at a platen speed of 15 mm/s. After the target radial expansion ratio was reached, the samples were held at 195 ℃ under pressure for 5 min, and then naturally cooled to room temperature. A schematic illustration of the hot-pressing process, together with the squeezing-flow velocity distribution and corresponding microstructural evolution of the composites, is shown in Fig. 1(b). In the cylindrical coordinate system, with the center of the cylindrical composite taken as the coordinate origin, the flow velocity $v_r(r, z, t)$[37] can be written as

$$v_r(r,z,t) = \frac{(2n+1)\left(-\dot{h}\right)^{\frac{1}{n}} r}{2h(n+1)}\left[1-\left(\frac{z}{h}\right)^{1+\frac{1}{n}}\right] \tag{1}$$

where t is the time, r and z represent the radial and axial coordinates, respectively, n is the non-Newtonian index, h is the thickness of the composite, and h denotes the closing rate of the two platens. The remaining symbols are shown in Fig. 1(b). The local shear rate associated with the squeezing flow can then be expressed as

$$\dot{\gamma} = \frac{\partial v_r(r,z,t)}{\partial z} = -\frac{(2n+1)\left(-\dot{h}\right)^{\frac{1}{n}} r z^{\frac{1}{n}}}{2n h^{2+\frac{1}{n}}} \tag{2}$$

As indicated by Eq. (2), the squeezing flow during hot pressing generates a nonuniform shear field, with the highest shear rate located near the platens. Such a flow field combines extensional and shear deformation, thereby driving the radial alignment of the hybrid nanofillers and cooperative rearrangement of the PA6 chains.

Characterization and Measurements

SEM and TEM were used to characterize the morphology of the hybrid nanofillers as well as the dispersion and orientation states of the nanofillers in the composites. SEM observations of the composites were performed using an Apreo 2S microscope (Thermo Fisher Scientific, USA). The samples were cryo-fractured in liquid nitrogen to expose fresh cross sections and then sputter-coated with gold prior to observation. The accelerating voltage was set to 10 kV. TEM characterization was performed using an HT-7800 microscope (Hitachi, Japan) at an accelerating voltage of 100 kV. For the hybrid nanofillers, a dilute dispersion was deposited onto the copper grids and dried naturally before observation. Ultrathin sections were prepared for the composites by cryo-ultramicrotomy using an EM UC7 ultramicrotome (Leica, Germany) and transferred onto copper grids for TEM observation.

Raman mapping measurements were carried out on a DXR2xi Raman imaging microscope (Thermo Fisher Scientific, USA) using a 785 nm laser as the excitation source to suppress fluorescence interference.

2D-WAXD measurements were carried out using a Xeuss 3.0 SAXS/WAXS system (Xenocs, France) equipped with an Eiger2R 1M detector with a pixel size of 75 μm. Cu Kα radiation with an X-ray energy of 8.05 keV (λ=1.54189 Å) was used, and all measurements were performed under vacuum conditions (<100 Pa). The two-dimensional scattering patterns were azimuthally integrated to obtain one-dimensional intensity-scattering vector (q) profiles, where the scattering vector q was calculated according to Eq. (3):

$$q = \frac{4\pi\sin\theta}{\lambda} \tag{3}$$

DSC was used to investigate the thermal transitions and crystallization behavior of the samples using a TGA/DSC 3+ synchronous thermal analyzer (Mettler Toledo, Switzerland). The measurements were performed under a nitrogen atmosphere by heating the samples from 30 ℃ to 250 ℃ at a rate of 10 ℃/min, followed by cooling to 30 ℃ at the same rate. The melting enthalpy (ΔH_m) obtained from the endothermic

melting peak during the heating scan was used to calculate the degree of crystallinity (X_c). X_c was determined assuming a melting enthalpy of 190 J/g for 100% crystalline PA6 (ΔH_m^∞)[38] according to the following relation:

$$X_c = \frac{\Delta H_m}{\Delta H_m^\infty} \times 100\% \quad (4)$$

PALS measurements were performed on a DPLS3000 spectrometer (ORTEC, USA) equipped with a ^{22}Na source to probe the free-volume features of the samples. The obtained spectra were subsequently analyzed using Melt 4.0 software.

Hydrogen permeability measurements were carried out using an SMT-275 gas permeation analyzer (Systester, China) at 23 °C under a test pressure of 0.1 MPa, according to GB/T 1038.1-2022. The hydrogen permeability coefficient (P) was calculated from the steady-state permeation data using

$$P = \frac{\Delta p}{\Delta t} \times \frac{V}{A} \times \frac{T_0}{p_0 T} \times \frac{d}{p_1 - p_2} = 1.1574 \times 10^{-11}\,\mathrm{GTR} \times d \quad (5)$$

where $\Delta p/\Delta t$ is the average pressure rise rate in the low-pressure chamber under steady-state permeation, V is the volume of the low-pressure chamber, A is the effective permeation area, T_0 and p_0 are the standard temperature and pressure, respectively, T is the test temperature, d is the average thickness of the specimen, p_1–p_2 is the pressure difference across the specimen, and GTR denotes the gas transmission rate. The permeability coefficient, P, was expressed in units of $cm^3 \cdot cm \cdot cm^{-2} \cdot s^{-1} \cdot Pa^{-1}$.

The tensile properties of the samples were evaluated using a universal testing machine (Instron 5569, Instron, USA). Rectangular specimens of dimensions 25 mm × 4 mm × 1 mm were tested at a crosshead speed of 8.3 $mm \cdot min^{-1}$. The through-plane and in-plane thermal conductivities of the samples were measured using a LFA-476 HT laser flash apparatus (Netzsch, Germany). For comparison, the ε=0 mechanical, thermal conductivity, and DSC data of neat PA6 and GO-*g*-CNT/PA6 used as reference baselines in this study were replotted from our previous study.[24]

RESULTS AND DISCUSSION

Morphology of GO-*g*-CNT Hybrid Nanofillers

Fig. 2 shows the TEM images of the GO, CNT, and GO-*g*-CNT hybrid nanofillers. As shown in Fig. 2(a), GO exhibits a typical thin and wrinkled sheet-like morphology with a relatively transparent contrast, indicating an ultrathin layered structure. Unlike GO, the pristine CNTs in Fig. 2(b) display a typical tubular morphology with a high aspect ratio and partial entanglement. After hybridization, the TEM image of GO-*g*-CNT in Fig. 2(c) shows the coexistence of sheet-like GO and tubular CNT structures within the same nanofiller. CNTs were closely associated with the GO sheets rather than existing as completely separated entities, suggesting the successful construction of the GO-*g*-CNT hybrid structure. This hybrid architecture is expected to combine the two-dimensional barrier effect of GO with the bridging role of CNT, which is beneficial for the subsequent formation of an interconnected nanofiller network in the PA6 matrix.

Hot-pressing Induced Orientation of Hybrid Nanofillers in PA6 Composites

Figs. 3(a)–3(c) show SEM images of neat PA6 at different ε values. Before hot pressing, the fractured surface exhibited a relatively disordered morphology. After hot pressing, a more layered and anisotropic texture gradually developed, indicating a pronounced rearrangement of the PA6 matrix under squeezing flow. The corresponding SEM images of the GO-*g*-CNT/PA6 composites are shown in Figs. 3(d)–3(f). Compared to the composite at ε=0, the hot-pressed samples exhibited a more obvious layered morphology, suggesting progressive microstructural reorganization during radial expansion. Among them, the composite at ε=2 shows a more distinctly oriented texture, whereas the sample at ε=4 exhibits a more compact layered morphology. More direct evidence of the orientation behavior of the hybrid nanofillers is provided by the TEM images in Figs. 3(g)–3(i). In the composite without hot-pressing, the hybrid nanofillers were distributed in a largely random manner. After hot pressing, both the GO sheets and CNTs exhibited preferential alignment along the flow direction, confirming that the squeezing flow can induce nanofiller reorientation within the PA6 matrix. This feature is more apparent for the composite at ε=2, where the aligned GO sheets and CNTs can be identified more clearly. In comparison, the orientation of the hybrid nanofillers is less pronounced at ε=4. In addition, the Raman G-band mapping indicated that the overall distribution state of the hybrid nanofillers remained largely unchanged after hot pressing (Fig. S1 in the electronic supplementary information, ESI). These results indicate that the primary effect of hot pressing is to induce nanofiller reorientation rather than markedly improve the dispersion state.

Orientation and Crystallization Behavior of PA6 and GO-*g*-CNT/PA6 Composites under Hot Pressing

The crystalline orientations of the neat PA6 and GO-*g*-CNT/PA6 composites under hot pressing were further investigated using 2D-WAXD, as shown in Fig. 4. The testing geometry is illustrated in Fig. 4(a), where the X-ray beam was incident on the cross section of the specimens to evaluate the crystalline orientation relative to the flow direction. The 2D-WAXD patterns of neat PA6 at different ε values are shown in Figs. 4(b1)–4(b3), while those of the GO-*g*-CNT/PA6 composites are presented in Figs.

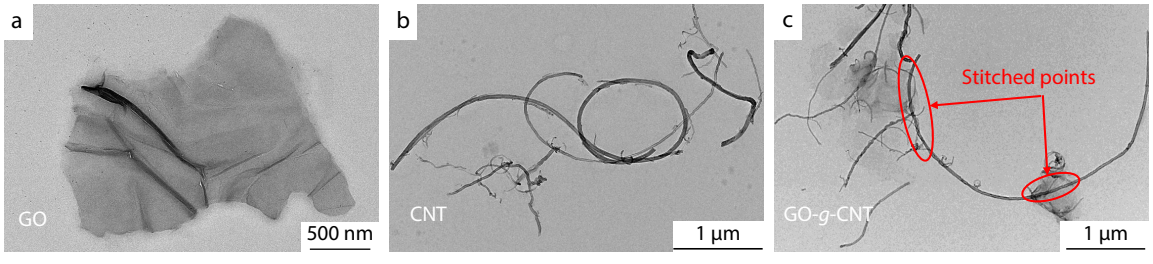

Fig. 2 TEM images of (a) GO, (b) CNT, and (c) GO-*g*-CNT hybrid nanofillers.

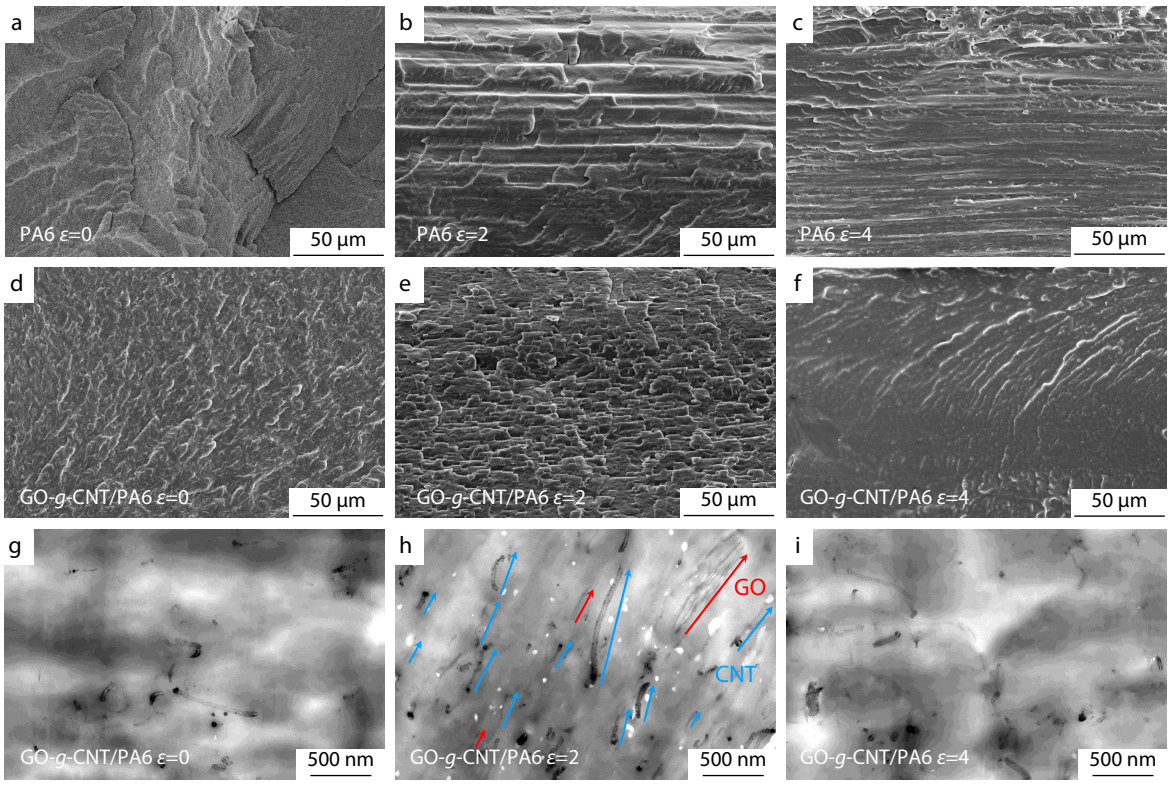

Fig. 3 SEM images of (a–c) neat PA6 and (d–f) GO-*g*-CNT/PA6 composites at ε=0, 2, and 4, respectively. (g–i) TEM images of GO-*g*-CNT/PA6 composites at ε=0, 2, and 4, respectively.

4(c1)–4(c3). For the samples that were not hot-pressed, the diffraction rings were nearly isotropic, indicating the absence of a pronounced crystalline orientation. Two main diffraction rings were identified and assigned to the α_1(200) and α_2(002)/(202) crystal planes of PA6, respectively.[39–41] After hot pressing, the isotropic diffraction rings gradually evolve into anisotropic arcs located at specific meridional and equatorial positions, indicating the development of a preferred crystalline orientation during hot pressing. The azimuthal intensity profiles extracted from the 2D-WAXD patterns are shown in Figs. 4(d) and 4(e). For the unoriented samples, the azimuthal curves are relatively flat, indicating an isotropic structure. After hot pressing, distinct intensity maxima appeared, and the peaks became progressively sharper, confirming the development of a crystalline orientation. The orientation degree was quantified using the Hermans orientation factor,[42] f, calculated from the azimuthal intensity distribution according to Eq. (6):

$$f = \frac{3\langle\cos^2\varphi\rangle - 1}{2} \tag{6}$$

where $\langle\cos^2\varphi\rangle$ is defined as:

$$\langle\cos^2\varphi\rangle = \frac{\int I(\varphi)\cos^2\varphi \mathrm{d}\varphi}{\int I(\varphi)\mathrm{d}\varphi} \tag{7}$$

Here, φ is the angle between the crystal orientation and reference direction, and $I(\varphi)$ is the corresponding azimuthal intensity. In this definition, f=1, 0, and –0.5 correspond to ideal parallel orientation, random orientation, and perpendicular orientation, respectively. As shown in Fig. 4(f), the Hermans orientation factor of neat PA6 increases from 0.22 at ε=0 to 0.68 at ε=2, and then decreases to 0.44 at ε=4, indicating that

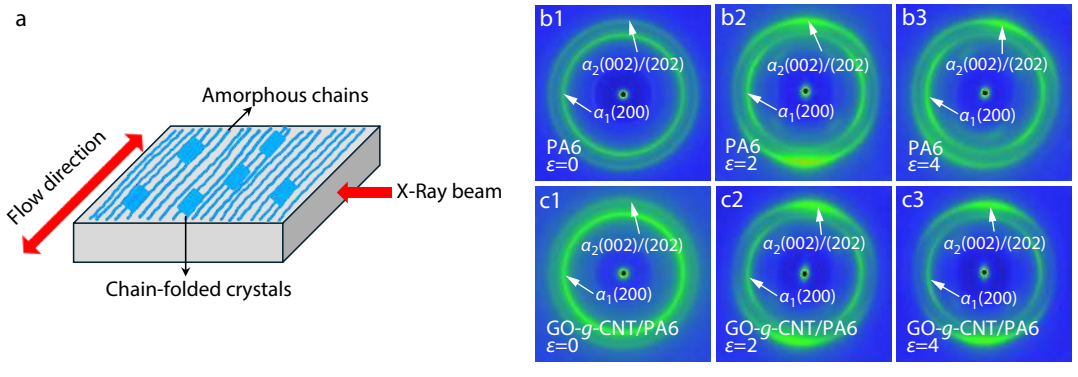

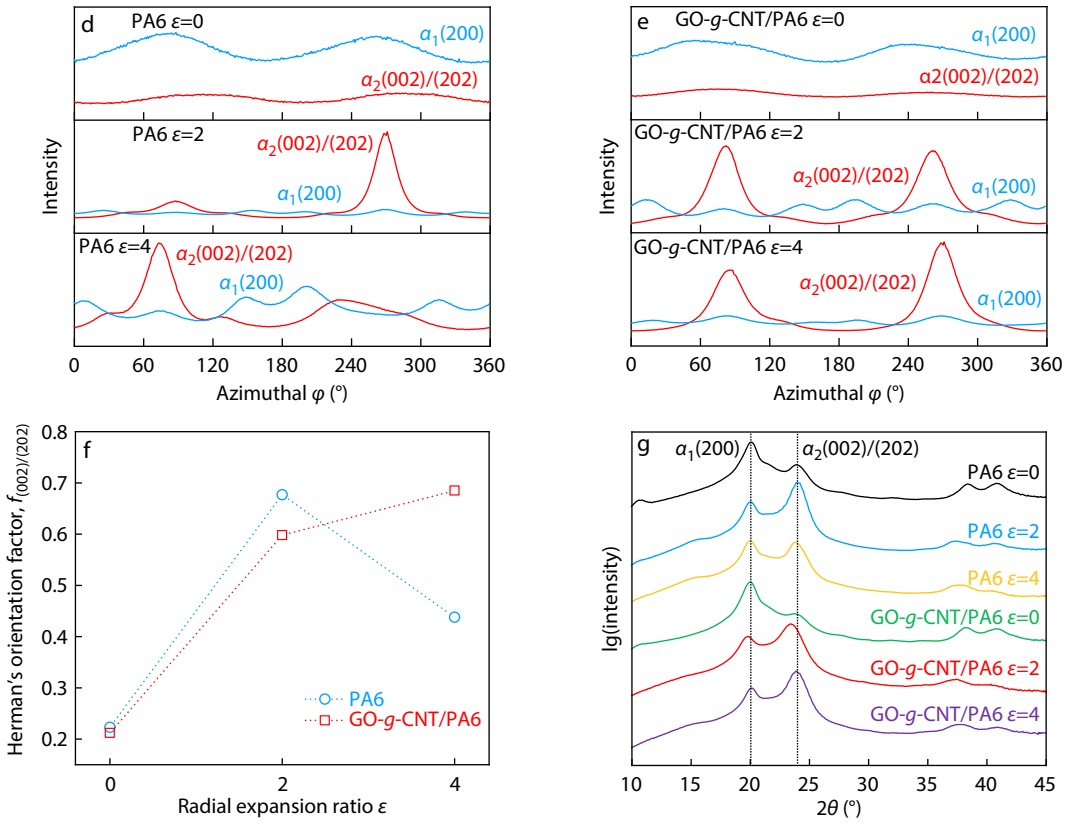

Fig. 4 (a) Schematic illustration of the 2D-WAXD testing geometry; (b1–b3) 2D-WAXD patterns of neat PA6 at ε=0, 2, and 4, respectively; (c1–c3) 2D-WAXD patterns of GO-*g*-CNT/PA6 composites at ε=0, 2, and 4, respectively; (d, e) Azimuthal intensity profiles of neat PA6 and GO-*g*-CNT/PA6 composites, respectively; (f) Hermans orientation factor of neat PA6 and GO-*g*-CNT/PA6 composites at different ε values; (g) One-dimensional intensity-2θ curves.

moderate hot pressing is most effective in inducing crystalline orientation in neat PA6. In contrast, the GO-*g*-CNT/PA6 composites exhibit a continuous increase in orientation factor from 0.21 at ε=0 to 0.60 at ε=2 and 0.69 at ε=4, suggesting that the hybrid nanofillers favor the retention and further development of crystalline orientation under stronger squeezing flow.

The corresponding one-dimensional intensity-2θ curves derived from the 2D-WAXD patterns are shown in Fig. 4(g). To better display the relatively weak wide-angle diffraction peaks, the intensities were plotted on a logarithmic scale. Two characteristic diffraction peaks were observed at approximately 20° and 24°, corresponding to the α_1(200) and α_2(002)/(202) reflections of PA6, respectively, confirming that the crystals remained in the α form after hot-pressing. With increasing ε, the α_2(002)/(202) reflection gradually becomes more prominent, suggesting that hot pressing alters the relative contribution of the α-form crystal planes to the diffraction.

The crystallization behavior of the neat PA6 and GO-*g*-CNT/PA6 composites before and after hot pressing was investigated by DSC, as shown in Fig. 5(a), and the corresponding crystallinity values are summarized in Fig. 5(b) and Table 1. For neat PA6, the crystallinity increased markedly from 25.4% at ε=0 to 44.8% at ε=2 and remained at a relatively high level of 41.1% at ε=4. A similar trend was observed for the composites, in which the crystallinity increased from 23.1% at ε=0 to 41.1% and 39.5% at ε=2 and 4, respectively. These results indicate that hot pressing significantly promoted crystallization in both neat PA6 and GO-*g*-CNT/PA6 composites, which can be attributed to the enhanced chain rearrangement and packing induced by the squeezing flow. Compared with neat PA6, the GO-*g*-CNT/PA6 composites exhibited substantially higher crystallization temperatures, with T_c values of approximately 187 °C, whereas those of neat PA6 were approximately 165–171 °C. This difference suggests that the hybrid nanofillers provided effective heterogeneous nucleation sites for PA6 crystallization.[43] However, the nucleation effect does not necessarily lead to higher final crystallinity. Polymer crystallization in nanocomposites is governed by both nucleation and subsequent crystal growth. In the present system, covalently bonded hybrid nanofillers can promote nucleation, but their strong interfacial interactions with PA6 chains and the geometric confinement introduced by the hybrid architecture may restrict chain diffusion, lamellar growth, and crystal perfection. As a result, the crystallinity of GO-*g*-CNT/PA6 remained slightly lower than that of neat PA6, although its T_c was markedly increased.[44–46] Meanwhile, the melting temperatures (T_m) of the composites were slightly lower than those of neat PA6, implying that the crystals formed in the presence of hybrid nanofillers were somewhat less perfect.[47,48]

Hydrogen Barrier Performance and Underlying Mechanism

The hydrogen barrier performance of the neat PA6 and GO-*g*-

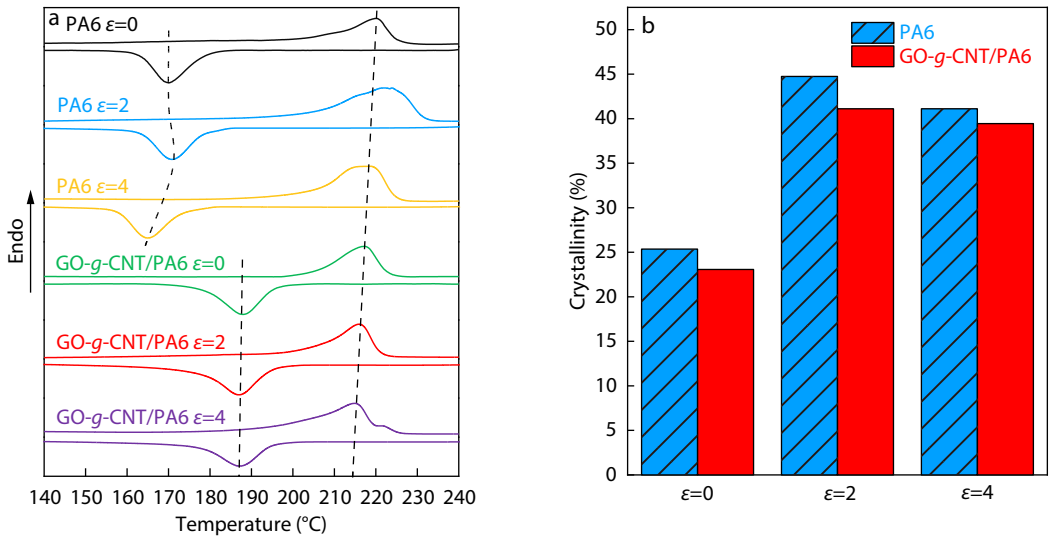

Fig. 5 (a) DSC heating and cooling curves of neat PA6 and GO-*g*-CNT/PA6 composites; (b) Crystallinity and crystallinity enhancement of neat PA6 and GO-*g*-CNT/PA6 composites at different ε values.

Table 1 DSC parameters of neat PA6 and GO-*g*-CNT/PA6 composites at different ε values.

Sample	ε	T_m (°C)	ΔH_m (J/g)	T_c (°C)	X_c (%)
PA6	0	219.8	48.2	170.2	25.4
	2	223.8	85.0	170.8	44.8
	4	218.8	78.1	165.0	41.1
GO-*g*-CNT/PA6	0	217.2	43.8	188.2	23.1
	2	216.0	78.1	187.0	41.1
	4	214.9	75.0	187.1	39.5

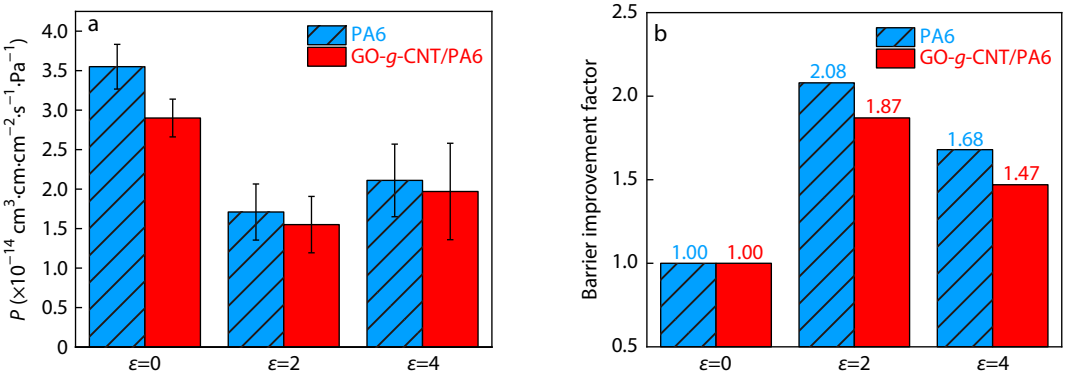

Fig. 6 (a) *P* values and (b) BIF of neat PA6 and GO-*g*-CNT/PA6 composites at different ε values.

CNT/PA6 composites at different ε values is shown in Fig. 6. For neat PA6, the hydrogen permeability coefficient *P* decreases from 3.55×10^{-14} $cm^3\cdot cm\cdot cm^{-2}\cdot s^{-1}\cdot Pa^{-1}$ at ε=0 to 1.71×10^{-14} $cm^3\cdot cm\cdot cm^{-2}\cdot s^{-1}\cdot Pa^{-1}$ at ε=2, and then slightly increases to 2.11×10^{-14} $cm^3\cdot cm\cdot cm^{-2}\cdot s^{-1}\cdot Pa^{-1}$ at ε=4. A similar trend is observed for the GO-g-CNT/PA6 composites, where *P* decreases from 2.90×10^{-14} $cm^3\cdot cm\cdot cm^{-2}\cdot s^{-1}\cdot Pa^{-1}$ at ε=0 to 1.55×10^{-14} $cm^3\cdot cm\cdot cm^{-2}\cdot s^{-1}\cdot Pa^{-1}$ at ε=2, followed by a slight increase to 1.97×10^{-14} $cm^3\cdot cm\cdot cm^{-2}\cdot s^{-1}\cdot Pa^{-1}$ at ε=4. These results indicate that hot pressing can markedly improve the hydrogen barrier performance of both neat PA6 and GO-*g*-CNT/PA6 composites, with ε=2 resulting in the lowest *P* in both systems.

The barrier improvement factor (BIF) was used to quantify the barrier enhancement induced by hot pressing and was defined as

$$\mathrm{BIF} = \frac{P_0}{P} \tag{8}$$

where P_0 and *P* are the hydrogen permeability coefficients of the unpressed and hot-pressed samples, respectively. According to this definition, the BIF values of neat PA6 are 2.08 and 1.68 at ε=2 and 4, respectively, while those of GO-*g*-CNT/PA6 are 1.87 and 1.47. The higher BIF at ε=2 confirms that moderate hot pressing is more effective than strong deformation in improving the hydrogen barrier performance. At the same ε, the *P* values of GO-*g*-CNT/PA6 remain lower than those of neat PA6, with $P_{PA6}/P_{composites}$ values of approximately 1.22, 1.10, and 1.07 at ε=0, 2, and 4, respectively. This indicates that the incorporation of GO-*g*-CNT hybrid nanofillers reduces the permeability base-

https://doi.org/10.1007/s10118-026-3765-8

line of the matrix before hot pressing, so that the composite retains lower absolute P values under all hot-pressing conditions, even though its relative BIF values are slightly lower than those of neat PA6.

A representative PALS analysis was performed for the GO-g-CNT/PA6 composites at ε=0 and 2 to clarify the structural origin of the barrier enhancement, as shown in Fig. 7. In the PALS spectra, the third lifetime component τ_3 is associated with the ortho-positronium lifetime in the free-volume holes, while the corresponding intensity I_3 reflects the relative population of these holes.[49] The free-volume hole radius (R) was estimated from τ_3 using the Tao-Eldrup model[50,51]:

$$\tau_3 = \frac{1}{2}\left[1 - \frac{R}{R+\Delta R} + \frac{1}{2\pi}\sin\left(\frac{2\pi R}{R+\Delta R}\right)\right]^{-1} \quad (9)$$

where ΔR=0.166 nm. The corresponding free-volume hole volume (V_f) was calculated as

$$V_f = \frac{4}{3}\pi R^3 \quad (10)$$

The fractional free volume (f_v) was estimated from V_f and I_3 using the standard empirical relation

$$f_v = C \cdot V_f \cdot I_3 \quad (11)$$

where C is the empirical constant. As shown in Fig. 7(a), the τ_3 values remain nearly unchanged at 1.63 ns for both samples, indicating that hot pressing does not significantly alter the characteristic size of the individual free-volume holes. Meanwhile, I_3 decreases from 19.70% to 17.90% after hot pressing. Consistently, the calculated free-volume hole radius remains nearly unchanged at about 2.48 Å, whereas the fractional free volume decreases from 1.26% to 1.15%, as shown in Fig. 7(b). These results suggest that hot pressing mainly reduces the overall population of free-volume holes, rather than substantially changing their individual sizes.

Therefore, the decrease in the hydrogen permeability can be attributed to several structural changes induced by hot pressing. SEM and TEM observations demonstrated the reorientation of the hybrid nanofillers, 2D-WAXD revealed enhanced crystalline orientation, DSC showed a clear increase in crystallinity, and PALS confirmed a reduction in the fractional free volume for the representative hot-pressed composite. These changes are expected to increase the tortuosity of the hydrogen diffusion and make the PA6 matrix more compact, thereby leading to the observed improvement in the hydrogen barrier performance.

Mechanical Properties and Thermal Conductivity

Fig. 8(a) shows representative tensile stress-strain curves, and Fig. 8(b) shows the average tensile strengths of the samples. For neat PA6, the tensile strength increases markedly from 39.8 MPa at ε=0 to 96.7 MPa at ε=2, corresponding to an increase of 143.0%, and remains at a similarly high level of 97.5 MPa at ε=4.

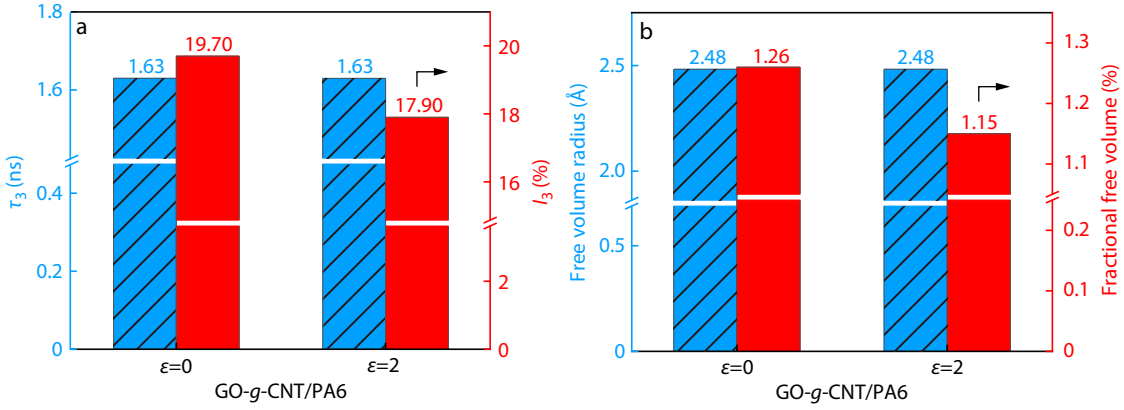

Fig. 7 Representative PALS analysis of GO-g-CNT/PA6 composites at ε=0 and 2. (a) τ_3 and its corresponding intensity I_3; (b) Calculated free-volume hole radius and fractional free volume.

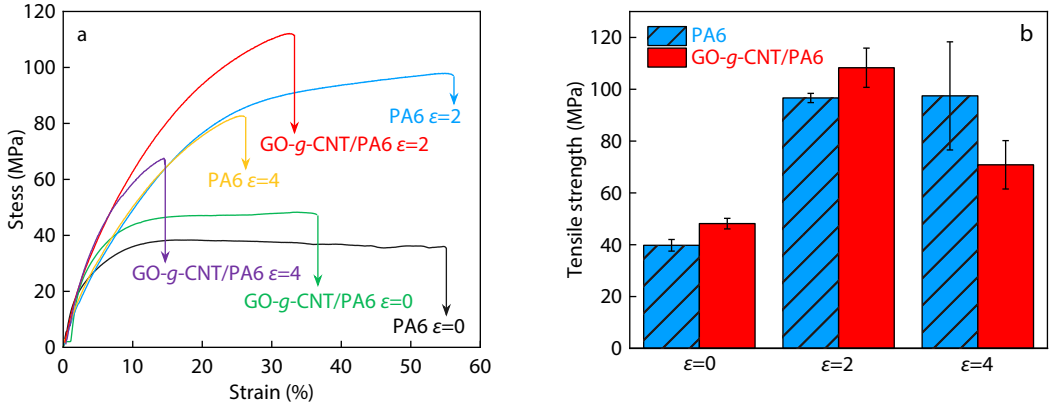

Fig. 8 Tensile properties of neat PA6 and GO-g-CNT/PA6 composites at different ε values: (a) representative tensile stress-strain curves; (b) average tensile strength.

https://doi.org/10.1007/s10118-026-3765-8

This pronounced improvement indicates that hot pressing effectively strengthened the PA6 matrix, which is consistent with the enhanced crystalline orientation and increased crystallinity revealed by the 2D-WAXD and DSC results. However, the stress-strain curves also show that the ductility of PA6 decreases after hot pressing, especially at ε=4, suggesting that stronger deformation leads to a more brittle response, even though the tensile strength remains high. Therefore, ε=2 provided a better balance between the strength and ductility of neat PA6.

The GO-*g*-CNT/PA6 composites exhibited higher tensile strengths than neat PA6 at ε=0 and 2, confirming the reinforcing effect of the hybrid nanofiller. Specifically, the tensile strength of the composite increases from 48.2 MPa at ε=0 to 108.3 MPa at ε=2, corresponding to an increase of 124.7%. This result indicates that moderate hot pressing is the most effective in establishing a favorable reinforcing microstructure. The superior tensile performance at ε=2 can be attributed to the more evident nanofiller alignment, improved load transfer between the nanofillers and the matrix, and the relatively high crystallinity achieved under this condition. When ε was further increased to 4, the tensile strength decreased markedly to 70.8 MPa. This result suggests that for the composite system, the tensile reinforcement is not governed solely by the crystalline orientation. Although the crystalline orientation was higher at ε=4, the nanofiller alignment observed by SEM and TEM appeared less distinct than that at ε=2, and the crystallinity was also slightly lower. In addition, the reduced elongation at break indicates a loss of deformability under stronger hot pressing. This decrease in ductility can be attributed to the stronger structural constraint generated by the excessive radial deformation. The more compact layered morphology and higher crystalline orientation at ε=4 may restrict the chain relaxation and plastic deformation during tensile loading. Meanwhile, the less distinct nanofiller alignment and slightly lower crystallinity are unfavorable for maintaining an efficient stress transfer and a balanced reinforcing structure. These factors are likely to promote earlier stress concentration and crack propagation during deformation, thereby weakening the reinforcement effect. Thus, ε=2 represents the optimal hot-pressing condition for GO-*g*-CNT/PA6 composites in terms of tensile performance.

The thermal conductivities of the neat PA6 and GO-*g*-CNT/PA6 composites at different ε values are shown in Fig. 9. For the ε=0 samples, no intentional orientation was introduced, and the measured thermal conductivity was used as an approximately isotropic reference in both the in-plane and through-plane directions. For neat PA6, the through-plane thermal conductivity increases from 0.229 W·m^{-1}·K^{-1} at ε=0 to 0.263 and 0.258 W·m^{-1}·K^{-1} at ε=2 and 4, respectively. The in-plane thermal conductivity showed a similar trend, increasing from 0.229 W·m^{-1}·K^{-1} at ε=0 to 0.264 and 0.267 W·m^{-1}·K^{-1} at ε=2 and 4, respectively. These results indicate that hot pressing can improve the thermal conductivity of neat PA6, which is consistent with the enhanced crystalline orientation and crystallinity after hot pressing. However, the difference between the in-plane and through-plane thermal conductivities remains small, indicating that the anisotropy of the thermal transport in neat PA6 is still limited.

The GO-*g*-CNT/PA6 composites exhibited consistently higher thermal conductivities than neat PA6 at the same ε,

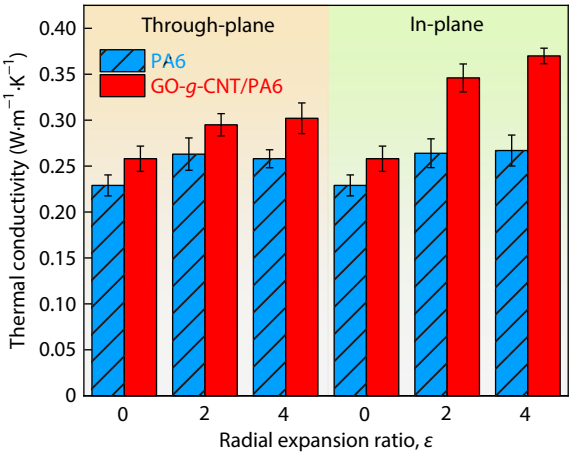

Fig. 9 Through-plane and in-plane thermal conductivities of neat PA6 and GO-*g*-CNT/PA6 composites at different ε values.

confirming the positive contribution of the hybrid nanofillers to heat transport. In the through-plane direction, the thermal conductivity of the composite increases from 0.258 W·m^{-1}·K^{-1} at ε=0 to 0.295 and 0.302 W·m^{-1}·K^{-1} at ε=2 and 4, respectively. A more pronounced enhancement was observed in the in-plane direction, where the thermal conductivity increased from 0.258 W·m^{-1}·K^{-1} at ε=0 to 0.346 W·m^{-1}·K^{-1} at ε=2 and further to 0.370 W·m^{-1}·K^{-1} at ε=4. This result indicated that hot pressing was particularly effective in improving in-plane heat transport in the composite system. This anisotropic enhancement can be attributed to the direction-dependent phonon transport pathways formed by the oriented hybrid nanofillers. During radial expansion, the GO sheets and CNTs tended to align preferentially in the in-plane direction. The aligned CNTs can act as one-dimensional thermal bridges between neighboring GO sheets, whereas the oriented GO sheets provide extended two-dimensional heat-spreading pathways. This hybrid arrangement reduces the discontinuity of phonon transport along the in-plane direction and facilitates more effective heat conduction. In contrast, heat transport in the through-plane direction still requires phonons to pass across polymer-rich regions and multiple matrix-nanofiller interfaces, where the interfacial thermal resistance remains relatively high. Therefore, the in-plane thermal conductivity was more sensitive to the nanofiller alignment induced by hot pressing than the through-plane thermal conductivity.

It is noteworthy that the optimal conditions for thermal conductivity differ from those for the tensile strength. Although the composite achieved the highest tensile strength at ε=2, the highest in-plane thermal conductivity was obtained at ε=4. This difference indicates that the microstructural requirements for the mechanical reinforcement and thermal transport are not identical. Moderate hot pressing is more favorable for achieving a balanced reinforcing structure, whereas stronger deformation appears to be more effective for establishing continuous in-plane heat conduction pathways.

CONCLUSIONS

In this study, the influence of hot pressing on the structural evo-

https://doi.org/10.1007/s10118-026-3765-8

lution and properties of GO-*g*-CNT/PA6 composites was systematically investigated. Hot pressing induced pronounced reorganization of the matrix and hybrid nanofillers, including more evident nanofiller alignment, enhanced crystalline orientation, increased crystallinity, and reduced fractional free volume in the representative composite sample. These structural changes effectively improved the hydrogen barrier, mechanical, and thermal transport properties. For hydrogen barrier performance, the permeability coefficient of PA6 decreased from 3.55×10^{-14} $cm^3\cdot cm\cdot cm^{-2}\cdot s^{-1}\cdot Pa^{-1}$ to 1.71×10^{-14} $cm^3\cdot cm\cdot cm^{-2}\cdot s^{-1}\cdot Pa^{-1}$ at ε=2, while that of GO-*g*-CNT/PA6 decreased from 2.90×10^{-14} $cm^3\cdot cm\cdot cm^{-2}\cdot s^{-1}\cdot Pa^{-1}$ to 1.55×10^{-14} $cm^3\cdot cm\cdot cm^{-2}\cdot s^{-1}\cdot Pa^{-1}$, corresponding to BIF values of 2.08 and 1.87, respectively. In terms of mechanical properties, the tensile strength of the composite increased from 48.2 MPa to 108.3 MPa at ε=2. Notably, the enhancement of the thermal transport became more pronounced in the in-plane direction, where the conductivity increased to 0.370 $W\cdot m^{-1}\cdot K^{-1}$ at ε=4. These results indicate that the optimal hot-pressing condition depends on the target property, with ε=2 being more favorable for the barrier and mechanical performance, whereas ε=4 is more effective for heat transport. This study clarifies the distinct roles of nanofiller alignment, crystalline orientation, crystallinity, and free volume in determining the structure-property relationships of hot-pressed GO-*g*-CNT/PA6 composites, which is valuable for the development of PA6-based liner materials for Type IV hydrogen storage vessels. Future work will further optimize hot pressing parameters to achieve a better balance among barrier, mechanical, and thermal transport properties, and will evaluate the long-term reliability of these composites under practical hydrogen storage conditions.

Conflict of Interests

The authors declare no interest conflict.

Electronic Supplementary Information

Electronic supplementary information (ESI) is available free of charge in the online version of this article at http://doi.org/10.1007/s10118-026-3765-8.

Data Availability Statement

Data supporting the findings of this study are available from the corresponding author upon reasonable request.

ACKNOWLEDGMENTS

This work was financially supported by the National Natural Science Foundation of China (No. 52502104), Shandong Provincial Natural Science Foundation (No. ZR2023QE311), Youth Innovation Support Program of Shandong Universities (No. 2024KJG083), Key R&D Program of Jiangxi Province (No. 20243BBG71003), and Jiangxi Provincial Natural Science Foundation (No. 20242BAB20167).

REFERENCES

1 Li, Y.; Xiao, Z.; Zhang, Y.; Li, W.; Zhang, W. Analysis of rapid decompression failure in polymer liner of Type IV hydrogen storage vessels using a novel fluid–solid coupling model. *Compos. Part A-Appl. Sci. Manuf.* **2025**, *188*, 108531.
2 Eko, A. J.; Epaarachchi, J.; Jewewantha, J.; Zeng, X. A review of type IV composite overwrapped pressure vessels. *Int. J. Hydrogen Energy* **2025**, *109*, 551–573.
3 Sun, W. X.; Li, Y. T.; Huang, W. J.; Zhang, Y. M.; Fan, M.; Xiao, Z. M.; Li, W. G. Advances in failure assessment of Type IV hydrogen storage vessels: a critical review. *Renew. Sust. Energy Rev.* **2026**, *226*, 116353.
4 Li, Y. T.; Huang, W. J.; Zhang, Y. M.; Fan, M.; Xiao, Z. M.; Li, W. G. Investigation of liner collapse behaviors in Type IV hydrogen storage vessels at different temperatures. *J. Energy Storage* **2025**, *129*, 117307.
5 Zhao, J.; Ding, G.; Feng, P.; Wu, C. High-pressure hydrogen effects on thermoplastics: a comprehensive review of permeation, decompression failure, and mechanical properties. *Adv. Ind. Eng. Polym. Res.* **2025**, *8*, 387–407.
6 Wu, X. Y.; Lin, J. L.; Xu, H. Y. Super tough polycaprolactam (PA6)-based blends with gas barrier properties. *Chinese J. Polym. Sci.* **2025**, *43*, 2403–2412.
7 Su, Y.; Lv, H.; Feng, C.; Zhang, C. Hydrogen permeability of polyamide 6 as the liner material of Type IV hydrogen storage tanks: A molecular dynamics investigation. *Int. J. Hydrogen Energy* **2024**, *50*, 1598–1606.
8 Piraino, F.; Pagnotta, L.; Corigliano, O.; Genovese, M.; Fragiacomo, P. Advances in type IV tanks for safe hydrogen storage: materials, technologies and challenges. *Hydrogen* **2025**, *6*, 80.
9 Liang, J.; Wu, Y.; Chen, Z.; Wu, T.; Li, Y.; Zhao, C.; Zhao, R.; Li, W. Comprehensive research on mechanical and gas barrier properties of nylon6 liner strengthened by multi-walled carbon nanotubes. *Mater. Today Commun.* **2024**, *41*, 111052.
10 Kis, D. I.; Kókai, E. A review on the factors of liner collapse in type IV hydrogen storage vessels. *Int. J. Hydrogen Energy* **2024**, *50*, 236–253.
11 Lu, Z.; Yang, Z.; Zhou, Q.; Zhang, Y.; Zhang, Y.; Zhu, Z.; Zhang, G.; Jiang, W.; Zhang, Y.; Huang, R.; Hu, Y. Enhanced gas and plasticizer barrier properties of silicone rubber with ordered functionalized magnetic graphene oxide. *ACS Appl. Nano Mater.* **2024**, *7*, 16330–16339.
12 Miah, M. R.; Ding, J.; Zhao, H.; Chu, Q.; Wang, H.; Wang, J.; Zhu, J. Boron nitride-based polyester nanocomposite films with enhanced barrier and mechanical performances. *ACS Appl. Polym. Mater.* **2024**, *6*, 2913–2923.
13 Marais, S.; Lozay, Q.; Follain, N.; Soulestin, J.; Couvrat, N.; Dargent, E. Multinanolayered PA6/cloisite and PE/PA6/cloisite composites: structure, mechanical and barrier properties. *Compos. Part B-Eng.* **2024**, *271*, 111167.
14 Zhang, P.; Wang, Q.; Zhang, Y.; Lin, M.; Zhou, X.; David, A.; Ustyuzhanin, A.; Chen, M.; Katsnelson, M. I.; Trubyanov, M.; Novoselov, K. S.; Andreeva, D. V. Strain-induced crumpling of graphene oxide lamellas to achieve fast and selective transport of H_2 and CO_2. *Nat. Nanotechnol.* **2025**, *20*, 1254–1261.
15 Yu, X.; Zhang, Y.; Fan, X.; Lv, Y.; Wang, Z.; Zhang, X.; Liu, T. Macromolecular PEI-modified carbon nanotubes as multifunctional additives in controlling crystallization and enhancing comprehensive performance of polyamide 6 nanocomposites. *Compos. Commun.* **2024**, *51*, 102057.
16 Sun, J.; Zhang, X.; Wang, Y.; Li, M.; Wei, X.; Liu, H.; Zhou, W. Experimental determination of the Young's modulus of individual single-walled carbon nanotubes with single chirality. *Nano Res.* **2024**, *17*, 7522–7532.

Graphical Abstract

Flow-induced Structural Evolution in Graphene Oxide-grafted Carbon Nanotube/Polyamide 6 Composites with Enhanced Barrier Performance, Mechanical Properties, and Thermal Conductivity

Guan-Jun Liu, Mei-Ling Yan, Zhen Tian, Lu Wang, Fan Yang, and Rong-Guo Wang

Shandong University of Aeronautics; Nanchang Hangkong University; Shanxi Institute of Energy; Harbin Institute of Technology

Flow-induced structural evolution regulates the barrier, mechanical, and thermal properties of the graphene oxide-grafted carbon nanotube/polyamide 6 (GO-*g*-CNT/PA6) composites. Moderate deformation favors a hydrogen barrier and tensile enhancement, whereas stronger deformation promotes in-plane heat transport.

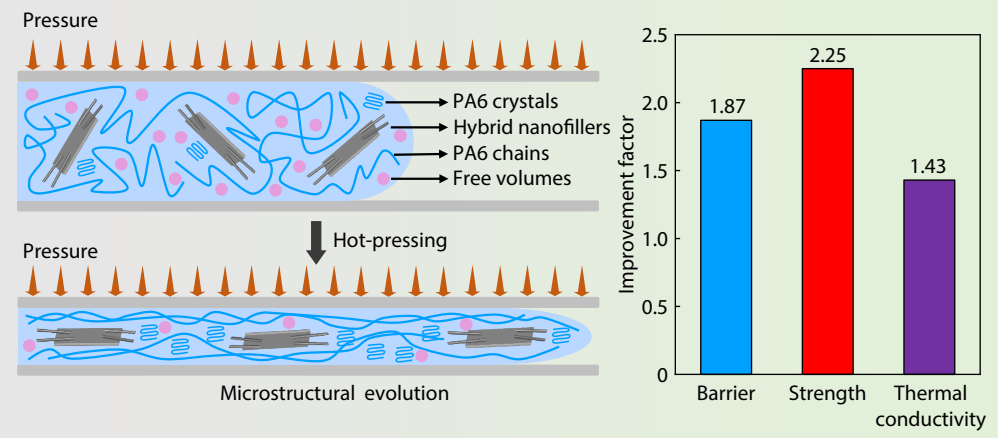

Chinese J. Polym. Sci., 2026 *https://doi.org/10.1007/s10118-026-3765-8*

17 Zeng, Z.; Wang, G.; Wolan, B. F.; Wu, N.; Wang, C.; Zhao, S.; Yue, S.; Li, B.; He, W.; Liu, J.; Lyding, J. W. Printable aligned single-walled carbon nanotube film with outstanding thermal conductivity and electromagnetic interference shielding performance. *Nano-Micro Lett.* **2022**, *14*, 179.

18 Liu, M.; Lin, K.; Zhou, M.; Wallwork, A.; Bissett, M. A.; Young, R. J.; Kinloch, I. A. Mechanism of gas barrier improvement of graphene/polypropylene nanocomposites for new-generation light-weight hydrogen storage. *Compos. Sci. Technol.* **2024**, *249*, 110483.

19 Yu, Z.; Zhang, C.; Chen, M.; Huang, J. Versatile phenolic composites by in situ polymerization of concentrated dispersions of carbon nanotubes. *PNAS Nexus* **2025**, *4*, pgaf274.

20 Du, H.; Chen, X.; Ding, H.; Yin, X.; Su, Y.; Weng, G. J. The effect of adding graphene oxide into CNT/polymer system on the CNT dispersion and mechanical properties of the hybrid nanocomposites. *Compos. Commun.* **2025**, *53*, 102196.

21 Liu, B.; Sun, J.; Zhao, J.; Yun, X. Hybrid graphene and carbon nanotube–reinforced composites: polymer, metal, and ceramic matrices. *Adv. Compos. Hybrid Mater.* **2024**, *8*, 1.

22 Zhang, B.; Dou, Z. L.; Zhang, Y. Z.; Fu, Q.; Wu, K. Exploring trade-offs in thermal interface materials: the impact of polymer-filler interfaces on thermal conductivity and thixotropy. *Chinese J. Polym. Sci.* **2024**, *42*, 916–925.

23 Díez-Pascual, A. M.; Luceño-Sánchez, J. A. Thermal and barrier properties of poly(3-hydroxybutyrate) hybrid nanocomposites: use of experimental data for reliable prediction *via* machine learning. *New J. Chem.* **2026**, *50*, 2332–2349.

24 Liu, G.; Liu, Y.; Zhang, M.; Zhao, D.; Liu, P.; Wang, L.; Li, L.; Yan, M. Covalently bonded graphene oxide–carbon nanotube hybrid nanofillers for achieving high-performance polyamide 6 composites with superior mechanical properties and thermal conductivity. *Nanoscale* **2025**, *17*, 18127–18142.

25 Klonos, P. A.; Bikiaris, R. D.; Terzopoulou, Z.; Mouchlianiti, K.; Tsachouridis, K.; Anastasiou, A. D.; Kyritsis, A.; Kyzas, G. Z. Structure-properties relationships in new polymer nanocomposites based on the renewable poly(butylene succinate) filled with low amounts of nanoparticles of 1-3D geometries. *Polymer* **2024**, *296*, 126841.

26 Huang, J.; Zhou, J.; Liu, M. Interphase in polymer nanocomposites. *JACS Au* **2022**, *2*, 280–291.

27 Liu, M.; Zhang, S.; Chen, Q.; Xie, Z.; Huang, Z. X.; Qu, J.-P. Toward excellent barrier performance for semicrystalline polyethylene terephthalate *via* controlling crystallinity and rigid amorphous fraction. *Macromolecules* **2024**, *57*, 7970–7979.

28 Phan, B. K.; Shen, K. H.; Gurnani, R.; Tran, H.; Lively, R.; Ramprasad, R. Gas permeability, diffusivity, and solubility in polymers: Simulation-experiment data fusion and multi-task machine learning. *npj Comput. Mater.* **2024**, *10*, 186.

29 Zhou, L.; Xu, P. P.; Ni, S. H.; Xu, L.; Lin, H.; Zhong, G. J.; Huang, H. D.; Li, Z. M. Superior ductile and high-barrier poly(lactic acid) films by constructing oriented nanocrystals as efficient reinforcement of chain entanglement network and promising barrier wall. *Chinese J. Polym. Sci.* **2022**, *40*, 1201–1212.

30 Niu, D. Y.; Xu, P. W.; Xu, S. J.; Li, J. X.; Yang, W. J.; Ma, P. M. Robust poly(glycolic acid) films with crystal orientation and

reinforcement of chain entanglement network. *Chin. J. Polym. Sci.* **2023**, *41*, 1093−1103.
31 Durand, T.; De Almeida, O. Influence of semi-crystalline microstructure on gas permeability of poly(ether-ketone-ketone). *Polymer* **2024**, *308*, 127349.
32 Ho, D. H.; Choi, Y. Y.; Ki, S. Y.; Kim, D. H.; Cho, J. H. Getting in line: Filler alignment strategies for anisotropic composite fabrication. *Compos. Part B-Eng.* **2025**, *305*, 112626.
33 Li, J.; Guan, T.; Zhang, Z.; Fu, Y. T.; Guo, F. L.; Huang, P.; Li, Z.; Li, Y. Q.; Fu, S. Y. Orientation of discontinuous fillers in polymer composites: modelling, characterization, control and applications. *Prog. Mater. Sci.* **2025**, *148*, 101360.
34 Song, N.; Wang, P.; Jin, L.; Zhang, F.; Wang, Z.; Ding, P. Tunable oriented cellulose/BNNSs films designed for high-performance thermal management. *Chem. Eng. J.* **2022**, *437*, 135404.
35 Song, N.; Zhang, F.; Cao, D.; Wang, P.; Ding, P. Bicontinuous laminated structure design of polypropylene/reduced graphene oxide hybrid films for thermal management. *Adv. Compos. Hybrid Mater.* **2022**, *5*, 2873−2883.
36 Sattar, S.; Bhagatji, J. D.; Nazmus Saquib, M.; Pedrazzoli, D.; Zhang, M.; Kravchenko, S. G.; Kravchenko, O. G. Influence of flow-induced polymorphism and fiber morphology on mechanical behavior in long discontinuous glass fiber polyamide composites. *Compos. Part A-Appl. Sci. Manuf.* **2024**, *185*, 108353.
37 Liu, G.; Yang, F.; Liu, W.; Bai, Y.; Han, C.; Jiao, W.; Wang, P.; Wang, R. Ultra-high gas barrier composites with aligned graphene flakes and polyethylene molecules for high-pressure gas storage tanks. *J. Energy Storage* **2021**, *40*, 102692.
38 Doležal, J.; Benešová, V.; Brožek, J. Preparation of polyamide 6 with reduced flammability by polymerization casting. *J. Therm. Anal. Calorim.* **2024**, *149*, 981−991.
39 Fredi, G.; Broggio, L.; Valentini, M.; Bortolotti, M.; Rigotti, D.; Dorigato, A.; Pegoretti, A. Decoding the interplay of mold temperature and catalysts concentration on the crystallinity and mechanical properties of anionic polyamide 6: a combined experimental and statistical approach. *Polymer* **2024**, *311*, 127562.
40 Ma, D. X.; Li, Z. Q.; Tang, K.; Gong, Z. L.; Shao, J. Y.; Zhong, Y. W. Nylons with highly-bright and ultralong organic room-temperature phosphorescence. *Nat. Commun.* **2024**, *15*, 4402.
41 Zhuang, Y. F.; Cao, X. Y.; Zhang, J. N.; Ma, Y. Y.; Shang, X. X.; Lu, J. X.; Yang, S. L.; Zheng, K.; Ma, Y. M. Monomer casting nylon/graphene nanocomposite with both improved thermal conductivity and mechanical performance. *Compos. Part A-Appl. Sci. Manuf.* **2019**, *120*, 49−55.
42 Kim, J.; Lee, S.; Park, M.; Kim, Y.; Cho, N.-J.; Ahn, H.; Ryu, D. Y. Depth-dependent structural analysis of polyolefin multilayer films using microbeam X-ray diffraction. *Polym. Test.* **2025**, *150*, 108928.
43 Zheng, L.; Wu, Y.; Wang, M.; Chen, X. Construction and performance of an interfacial layer in carbon fiber/polyamide composites *via* electrostatic self-assembly. *Langmuir* **2026**, *42*, 2256−2269.
44 Jimenez, A. M.; Altorbaq, A. S.; Müller, A. J.; Kumar, S. K. Polymer crystallization under confinement by well-dispersed nanoparticles. *Macromolecules* **2020**, *53*, 10256−10266.
45 Wurm, A.; Ismail, M.; Kretzschmar, B.; Pospiech, D.; Schick, C. Retarded crystallization in polyamide/layered silicates nanocomposites caused by an immobilized interphase. *Macromolecules* **2010**, *43*, 1480−1487.
46 Liu, G.; Zhang, M.; Liu, Y.; Zhao, D.; Liu, Y.; Tian, Z.; Liu, P.; Wang, L.; Li, L.; Yan, M. Interface-engineered functionalized graphene oxide reinforced polyamide 6 composites with enhanced mechanical and thermal properties. *Polymer* **2025**, *335*, 128849.
47 Ge, F. F.; Du, J. H.; Yao, W. H.; Suntamit, B.; Wu, C.-S.; Potiyaraj, P.; Ma, Z. L.; Preuksarattanawut, C.; Bai, Y. S.; Tsou, C. H. Enhanced mechanical, thermal, barrier, and antibacterial properties of polypropylene nanocomposites reinforced with nano-silver carbon black. *Polym. Eng. Sci.* **2025**, *65*, 1549−1566.
48 Simaafrookhteh, S.; Van Thillo, T.; Lomov, S. V.; Ivens, J. Crystallinity of neat and carbon fiber-reinforced polyamide-6 processed at different cooling rates. *Compos. Part A-Appl. Sci. Manuf.* **2025**, *188*, 108520.
49 Consolati, G.; Nichetti, D.; Quasso, F. Probing the free volume in polymers by means of positron annihilation lifetime spectroscopy. *Polymers* **2023**, *15*, 3128.
50 Choudalakis, G.; Gotsis, A. D.; Schut, H.; Picken, S. J. The free volume in acrylic resin/laponite nanocomposite coatings. *Eur. Polym. J.* **2011**, *47*, 264−272.
51 Pethrick, R. A. Positron annihilation—a probe for nanoscale voids and free volume. *Prog. Polym. Sci.* **1997**, *22*, 1−47.